

Efficient Computation of Spatially-Discrete Traveling-Wave Modulated Structures

Cody Scarborough, *Member, IEEE*, Zhanni Wu, *Member, IEEE*, and Anthony Grbic, *Fellow, IEEE*

Abstract—Traveling-wave modulation is a form of space-time modulation which has been shown to enable unique electromagnetic phenomena such as non-reciprocity, beam-steering, frequency conversion, and amplification. In practice, traveling-wave modulation is achieved by applying a staggered time-modulation signal to a spatially-discrete array of unit cells. Therefore, the capability to accurately simulate spatially-discrete traveling-wave modulated structures is critical to design. However, simulating these structures is challenging due to the complex space-time dependence of the constituent unit cells. In this paper, a field relation (referred to as the interpath relation) is derived for spatially-discrete traveling-wave modulated structures. The interpath relation reveals that the field within a single time-modulated unit cell (rather than an entire spatial period) is sufficient to determine the field solution throughout space. It will be shown that the interpath relation can be incorporated into existing periodic method of moments solvers simply by modifying the source basis functions. As a result, the computational domain is reduced from an entire spatial period to a single time-modulated unit cell, dramatically reducing the number of unknowns. In the context of traveling-wave modulation, this enables researchers to efficiently simulate both complex structures with patterned unit cells in addition to continuous structures with infinitesimal unit cells.

Index Terms—Spatially-discrete traveling-wave modulation, traveling-wave modulation, method of moments, N-path networks, interpath relation, space-time modulation, metasurfaces, frequency-domain methods, periodic structures, computational techniques.

I. INTRODUCTION

SPACE-TIME modulation has attracted renewed interest within the field of electrodynamics. Progress in the availability/performance of tunable components and materials has drawn researchers to examine time and space-time variation as a means to achieve frequency conversion [1]–[5], amplification [6]–[8] and non-reciprocity [9]–[12]. In the late 1950s traveling-wave ferromagnetic amplifiers were explored by P. Tien and H. Suhl [6]. In [6], it was shown that amplification and frequency conversion can be simultaneously achieved by applying a traveling-wave modulation of permeability to a coupled-line system. Leading into the 1960s, E. Cassedy and A. Oliner examined the dispersion relations that arose from a medium whose permittivity is modulated by a traveling-wave

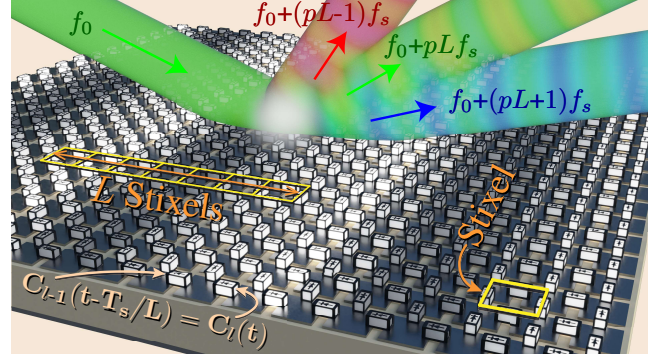


Fig. 1: Illustration of a spatially-discrete traveling-wave modulated structure [1]. Each spatial period is made up of L “stixels” (indivisible unit cells). In this example, the structure consists of metallic patches interconnected by varactor diodes placed above a grounded dielectric substrate. The varactor diodes are modulated in the form of spatially-discrete traveling-wave. That is, the varactor capacitance $C_l(t)$ within stixel l is delayed in time with respect to the previous stixel $l - 1$. When the spatial period is sufficiently small and the modulation frequency $f_s = 1/T_s$ is low, frequencies separated by pLf_s ($p \in \mathbb{Z}$) all propagate in the same direction.

[5]. Similar to coupled-mode theory applied to multiconductor transmission lines [13], the stop bands of the modulated structure were attributed to co-directional or contra-directional coupling. However, rather than coupling between transmission lines, the energy couples between frequency harmonics [5].

As the performance of tunable elements such as varactor diodes, electro/acousto/magneto-optic media, phase-change materials, and 2D materials has improved, researchers have begun implementing and expanding the theory of space-time modulated media [14]. This has led to the study of space-time modulated metasurfaces [1]–[3], [10], [11], [15]. In these structures, tunable components are arranged or patterned onto a surface or a stack of surfaces. In particular, significant attention has been paid to the capabilities of traveling-wave modulated metasurfaces [1], [10], [11], [16]–[20] such as the structure depicted in Fig. 1. In the continuous limit (i.e. the modulation is a continuous function of space and time), the behavior of traveling-wave modulated metasurfaces can often be predicted analytically via the Lorentz transform [21]. However, in practice, traveling-wave modulation is often achieved via staggered modulation of an array of discrete unit cells. We will refer to such a configuration as spatially-discrete traveling-wave modulation (SD-TWM). In this configuration,

C. Scarborough is with the Department of Electrical Engineering and Computer Science, University of Michigan, 1301 Beal Avenue, Ann Arbor, MI 48109-2122, USA (e-mail: codyscar@umich.edu).

Z. Wu is with the Department of Electrical Engineering and Computer Science, University of Michigan, 1301 Beal Avenue, Ann Arbor, MI 48109-2122, USA (e-mail: zhanni@umich.edu).

A. Grbic is with the Department of Electrical Engineering and Computer Science, University of Michigan, 1301 Beal Avenue, Ann Arbor, MI 48109-2122, USA (e-mail: agrbic@umich.edu).

the individual time-modulated unit cells are referred to as stixels [22]: space-time pixels. The discrepancy in the response between the continuous and discrete model has been generally overlooked in design. The biasing networks and fine features within the unit cells are typically only considered in a full-wave simulation just before fabrication.

The design of traveling-wave modulated metasurfaces has disrupted the traditional workflow of RF engineers and scientists. Typically, the theoretical performance of a physical device or idealized structure can be optimized and validated using a full-wave solver or circuit simulator. A large body of work has gone into the development of numerical methods, and commercial solvers have become a critical ally to pencil and paper. However, SD-TWM structures often require complicated biasing networks and extreme temporal variation. From a computational standpoint, this is problematic since most commercial solvers are not optimized to solve problems which are varying in both space and time. While modern numerical techniques (such as finite-difference time-domain method and harmonic-balance) can be used to solve space-time-dependent problems [3], [16]–[18], the computational cost to maintain sufficient numerical accuracy can be prohibitive. Further, physical patterned unit cells cannot be easily included in the techniques presented in [3], [17].

In this paper, we take advantage of the space-time symmetry of SD-TWM structures to dramatically reduce the computational cost of a full-wave simulation. A boundary condition (referred to as the interpath relation) between the stixels of a SD-TWM structure is derived and incorporated into a method of moments (MoM) solver. In Section II, a derivation of the interpath relation is provided. In Section III, the interpath relation is applied to a MoM formulation for the problem of a SD-TWM sheet capacitance over a grounded dielectric. The numerical results of this implementation are reported in Section IV. The conclusion is presented in Section V.

II. THE INTERPATH RELATION FOR SPATIALLY-DISCRETE TRAVELING-WAVE MODULATION

The staggered modulation scheme used to achieve SD-TWM is reminiscent of N-path circuit networks. An N-path network contains a set of linear, periodically time-varying (LPTV) systems (paths) connected to an input and output in parallel [23]. The defining characteristic of an N-path network is that the time-variation of each path is delayed with respect to the previous path. This means that if a time-varying component (say a time-varying capacitor) on the first path has time dependence $C_0(t)$, then the time dependence on path l is $C_0(t - lT_s/L)$, where T_s is the modulation period and L is the number of paths in parallel.

In [23], a relation was derived between the voltages and currents on each path of an N-path circuit network. When the network is excited by a time harmonic signal at frequency ω_0 , the time-domain relation between the voltage on each path, $v_l(t)$, is given by [23]

$$v_l(t) = e^{j\omega_0 t_0} v_{l-1}(t - t_0), \quad (1)$$

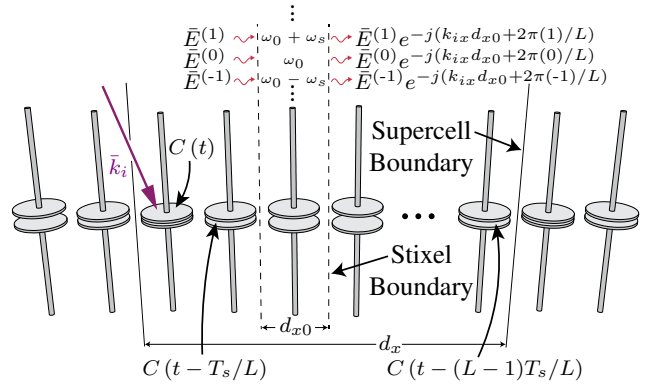


Fig. 2: An infinite array of capacitively loaded dipoles modulated in the form of a spatially-discrete traveling-wave. The structure is illuminated by a plane wave at frequency f_0 with an incident wavenumber \bar{k}_i . The solid black lines denote the boundaries of a supercell while the dashed lines denote the boundaries of a stixel. The frequency-domain form of the interpath relation derived in Section II is shown relating the frequency harmonics of the fields on the left and right boundaries of a stixel.

where $t_0 = T_s/L$. The same relation holds for the current on each path. Further, since the system is LPTV, the voltage can be expanded into harmonics of the form [24]

$$v_l(t) = \sum_{\nu=-\infty}^{\infty} V_l^\nu e^{j(\omega_0 + \nu\omega_s)t}. \quad (2)$$

Substituting this expansion in (1) yields

$$V_l^\nu = e^{-j2\pi\nu/L} V_{l-1}^\nu. \quad (3)$$

From this expression, it can be seen that the N-path modulation induces a phase shift of $-2\pi\nu/L$ between the paths for the ν^{th} harmonic.

Next, the interpath relation reported in [23] for N-path circuit networks will be extended to SD-TWM structures. The implications and applications of the interpath relation will then be examined.

A. Proof of the Interpath Relation

In this section, the interpath relation [20] is derived for the case of a plane wave incident upon a SD-TWM structure. As an example, consider the array of capacitively loaded dipoles shown in Fig. 2. The capacitance loading each dipole is a periodic function in time with period T_s . Further, the structure is spatially periodic along x with period d_x . A single spatial period is referred to as a supercell. Supercells are made up of L sub-domains referred to as stixels, each having a width of d_{x0} . The temporal variation of the capacitor within stixel l is related to that within stixel $l - 1$ via

$$C_l(t) = C_{l-1}(t - t_0), \quad (4)$$

where $t_0 = T_s/L$. From this expression, we observe that the variation of each capacitor is staggered in time, just as in the case of N-path circuit networks. We will now consider two

cases of plane wave illumination. In case A, the incident field is given by

$$\bar{\mathcal{E}}_i^A(\bar{r}, t) = \bar{E}_0 e^{j(\omega_0 t - \bar{k}_i \cdot \bar{r})}, \quad (5)$$

where $\bar{k}_i = k_{ix}\hat{x} + k_{iy}\hat{y} + k_{iz}\hat{z}$. Meanwhile, in case B, the incident field is given by

$$\begin{aligned} \bar{\mathcal{E}}_i^B(x, y, z, t) &= \bar{\mathcal{E}}_i^A(x - d_{x0}, y, z, t - t_0) \\ &= e^{-j(\omega_0 t_0 - k_{ix} d_{x0})} \bar{\mathcal{E}}_i^A(\bar{r}, t). \end{aligned} \quad (6)$$

We then define the total fields for cases A and B as $\bar{\mathcal{E}}^A(\bar{r}, t)$ and $\bar{\mathcal{E}}^B(\bar{r}, t)$ respectively. Since the system is linear, we note that

$$\bar{\mathcal{E}}^B(x, y, z, t) = e^{-j(\omega_0 t_0 - k_{ix} d_{x0})} \bar{\mathcal{E}}^A(x, y, z, t). \quad (7)$$

Further, by shifting the space-time coordinate system in case B from (x, y, z, t) to (x', y, z, t') , such that $x' = x - d_{x0}$ and $t' = t - t_0$, case A is reproduced. This implies

$$\begin{aligned} \bar{\mathcal{E}}^B(x, y, z, t) &= \bar{\mathcal{E}}^A(x', y, z, t') \\ &= \bar{\mathcal{E}}^A(x - d_{x0}, y, z, t - t_0). \end{aligned} \quad (8)$$

Equating the right-hand sides of (7) and (8), we obtain

$$e^{-j(\omega_0 t_0 - k_{ix} d_{x0})} \bar{\mathcal{E}}^A(x, y, z, t) = \bar{\mathcal{E}}^A(x - d_{x0}, y, z, t - t_0). \quad (9)$$

Thus, when a SD-TWM structure is excited by a plane wave, the total fields satisfy

$$\bar{\mathcal{E}}(x, y, z, t) = e^{j(\omega_0 t_0 - k_{ix} d_{x0})} \bar{\mathcal{E}}(x - d_{x0}, y, z, t - t_0). \quad (10)$$

This expression represents the time-domain interpath relation for SD-TWM structures. Since the system is LPTV, the fields throughout space can be expanded into frequency harmonics as [24]

$$\bar{\mathcal{E}}(\bar{r}, t) = \sum_{\nu=-\infty}^{\infty} \bar{E}^\nu(\bar{r}) e^{j(\omega_0 + \nu\omega_s)t}. \quad (11)$$

Substituting this expansion into (10) yields

$$\bar{E}^\nu(x, y, z) = e^{-j(k_{ix} d_{x0} + 2\pi\nu/L)} \bar{E}^\nu(x - d_{x0}, y, z). \quad (12)$$

This expression is the frequency-domain interpath relation for SD-TWM structures. The interpath relation reveals that, similar to an N-path network, the fields within neighboring stixels at frequency $f_0 + \nu f_s$ differ by a phase shift of $-2\pi\nu/L$ (in addition to the phase shift of the incident wave). This can be interpreted as an additional frequency-harmonic-dependent tangential momentum imparted by the modulation onto the field. Equation (12) can also be understood as a modified Floquet boundary condition which accounts for the space-time periodicity of the modulation.

B. Array Interpretation of the Interpath Relation

The interpath relation in (12) provides insight into the scattering behavior of SD-TWM structures. Let us consider the array factor produced by a single supercell of scatterers, as shown in Fig. 3 [19]. From (12), the array factor for frequency $f_0 + \nu f_s$ at observation positions in the x - z plane is given by

$$\text{ARFAC}(\theta_s) = \sum_{l=0}^{L-1} e^{jl(-k_{ix} d_{x0} - \frac{2\pi\nu}{L} + \frac{\omega_0 + \nu\omega_s}{c} d_{x0} \sin \theta_s)}, \quad (13)$$

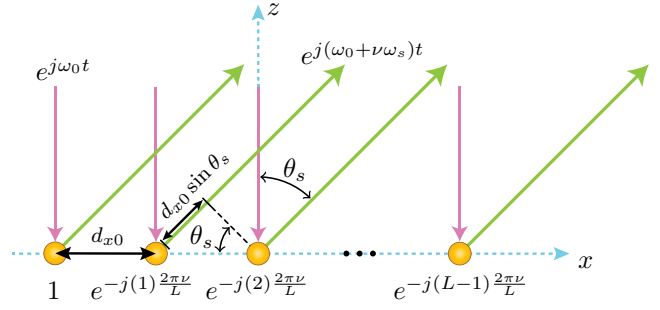


Fig. 3: Array interpretation of the scattering due to a single supercell consisting of L stixels for a given observation angle, θ_s , and observation frequency $f_0 + \nu f_s$. In this example, the monochromatic illumination at frequency f_0 is assumed to be normally incident ($k_{ix} = k_{iy} = 0$). Therefore, the relative phase of each source is given solely by the phase imparted by the modulation.

where θ_s is the observation angle with respect to the z axis. The relative phase of the excitation on each scatterer is determined by the incident angle and the particular frequency of observation. The inter-element phase due to the incident wave is $k_{ix} d_{x0}$. Meanwhile, the inter-element phase induced by the SD-TWM is $2\pi\nu/L$, where ν corresponds to the observed frequency of $f_0 + \nu f_s$.

For simplicity, let us focus on the array factor when the excitation is normally incident ($k_{ix} = k_{iy} = 0$). In this case, the array factor can be written as

$$\text{ARFAC}(\theta_s) = \sum_{l=0}^{L-1} e^{jl(-\frac{2\pi\nu}{L} + \frac{\omega_0 + \nu\omega_s}{c} d_{x0} \sin \theta_s)}. \quad (14)$$

From antenna array theory and (14), the beam-pointing direction(s) is dependent on the frequency harmonic and satisfies [25]

$$\frac{\omega_0 + \nu\omega_s}{c} d_{x0} \sin \theta_s = \frac{2\pi\nu}{L} + 2\pi p, \quad (15)$$

where p is an integer. If the modulation frequency is much smaller than the RF carrier frequency, then $\omega_0 + \nu\omega_s \approx \omega_0$. In this case, when ν is replaced by $\nu + L$, the beam-pointing angle(s) remains the same (since we are free to select p). This reveals that frequencies separated by $p'L f_s$ ($p' \in \mathbb{Z}$) are scattered to the same angle (or multiple angles). This effect, shown pictorially in Fig. 1, is not predicted when idealized continuous traveling-wave modulation is assumed [5]. Equation (15) also reveals that if

$$\frac{\omega_0 + \nu\omega_s}{c} d_{x0} < \left| \frac{2\pi\nu}{L} + 2\pi p \right|, \quad \forall p \in \mathbb{Z}, \quad (16)$$

then frequency $f_0 + \nu f_s$ does not correspond to any propagating angles. Frequencies which satisfy this condition are bound to the nearfield of the metasurface. A further discussion on the scattering behavior of SD-TWM is provided in [1].

C. Applications of the Interpath Relation

The interpath relation provides valuable insight into the behavior of SD-TWM structures. It reveals the potential for

these structures to achieve unique electromagnetic phenomena, such as sub-harmonic mixing and retro-reflective frequency conversion, as explored in [1]. By appropriately tailoring the time-dependence of a SD-TWM structure (e.g. Fig. 1), the frequency of the reflected wave can be shifted by an integer multiple of Lf_s , where L is the number of stixels per period. This effect is known as sub-harmonic mixing since the reflected wave is shifted by an integer multiple of f_s . Further, antenna array theory and (13) can be used to compute the required angle of incidence and L such that the scattered wave reflects back toward the illumination source at a translated frequency (i.e. retro-reflective frequency conversion). Finally, for structures designed theoretically via a continuous traveling-wave model, (15) can be used to find the maximum unit cell size such that grating lobes are not produced at any frequency in the physical implementation. This is particularly important when the modulation frequency, f_s , is comparable to the RF carrier frequency, f_0 .

In addition to providing physical understanding, the interpath relation can be used in practice to enable the simulation of SD-TWM structures. For both physical and idealized models, this relation will be shown in Section III to dramatically reduce the number of unknowns required to simulate these structures. The reduction in unknowns comes at no cost to the accuracy of the simulation since the interpath relation contains no approximations. For complicated unit cell designs which require a high level of discretization, the ability to simulate a single stixel can be a dramatic improvement over the simulation of several time-varying unit cells simultaneously. Further, idealized designs obtained via a continuous traveling-wave modulation model (such as those discussed in [10]–[12], [16]–[18]) can also benefit from a reduction in the number of unknowns required for simulation. This is because the stixel size for these structures can be made arbitrarily small. Without using the interpath relation, numerically simulating a continuous traveling-wave modulated structure would require the space-time variation to be discretized into individual time-varying computational elements over an entire spatial period [3], [26]. Using the interpath relation, we can shrink the computational domain to the width of a single computational element. This reduces the number of unknowns by the number of elements used in the simulation without the interpath relation.

III. METHOD OF MOMENTS FORMULATION USING THE INTERPATH RELATION

In this section we will derive the MoM formulation for a representative SD-TWM structure. We will begin by deriving the MoM formulation for the time-invariant structure shown in Fig. 4. The formulation for the time-invariant case will then be modified to account for SD-TWM. Specifically, in Section III-A, the MoM formulation will be derived for a periodic, inhomogeneous, time-invariant impedance sheet placed above a grounded dielectric substrate. In Section III-B, the time-invariant MoM formulation from Section III-A will be modified to account for a SD-TWM impedance sheet.

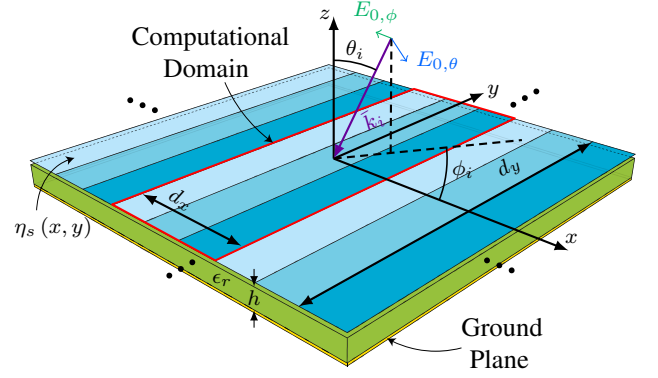


Fig. 4: An illustration of a plane wave incident upon an inhomogeneous impedance sheet placed over a grounded dielectric. Since the structure is periodic in space, the computational domain contains a single spatial period. It should be noted that this is just one example of a 2D spatially periodic impedance sheet. The presented formulation is valid for periodic variations along y , although this is not depicted in the figure.

A. Inhomogeneous Time-Invariant Structure

Here, we will derive the MoM formulation for the time-invariant structure shown in Fig. 4 under a plane-wave illumination. The isotropic sheet impedance placed on the surface of the grounded dielectric, $\eta_s(x, y)$, is periodic in x with period d_x and in y with period d_y . The dielectric has a relative permittivity of ϵ_r and a thickness of h . The excitation field phasor is a plane wave of the form

$$\begin{aligned} \bar{E}_i(\bar{r}) &= \bar{E}_0 e^{-j\bar{k}_i \cdot \bar{r}} \\ &= \bar{E}_0 e^{-j(k_{ix}x + k_{iy}y + k_{iz}z)} \\ &= \bar{E}_0 e^{jk_0(\sin\theta_i \cos\phi_i x + \sin\theta_i \sin\phi_i y + \cos\theta_i z)}. \end{aligned} \quad (17)$$

The procedure used here to obtain the MoM matrix equation closely follows the formulation presented by Jin in [27] for simulating a planar array of metallic patches.

First, we will write the boundary condition for the total field on the impedance sheet and subsequently express the scattered electric field in terms of the surface current density. The boundary condition at $z = 0$ is

$$\bar{E}_t(x, y) = \eta_s(x, y) \bar{J}_s(x, y), \quad (18)$$

where $\bar{E}_t(x, y)$ denotes the transverse component of the total electric field in the x - y plane. The total electric field can be separated into the incident field produced in the absence of the impedance sheet and the field scattered by the currents induced on the impedance sheet. Note that the incident field in the absence of the impedance sheet contains both the excitation field and the field reflected from the grounded dielectric. On the surface of the grounded dielectric, the reflected electric field can be written as

$$\bar{E}_{r,t}(x, y) = \bar{\Gamma} \bar{E}_{i,t}(x, y), \quad (19)$$

where $\vec{\Gamma}$ is the dyadic reflection coefficient which is a function of θ_i , ϕ_i , h and ϵ_r . By splitting the total electric field into incident and scattered components, (18) can be rewritten as

$$\left[1 + \vec{\Gamma}\right] \vec{E}_{i,t}(x, y) + \vec{E}_{s,t}(x, y) = \eta_s(x, y) \vec{J}_s(x, y), \quad (20)$$

where $\vec{E}_{i,t}$ and $\vec{E}_{s,t}$ denote the transverse components of the excitation and scattered electric field respectively. Since the structure is periodic in x and y , it follows from Floquet's Theorem that

$$\vec{J}_s(x, y) = e^{-j(k_{ix}x + k_{iy}y)} \vec{j}_s(x, y), \quad (21)$$

such that $\vec{j}_s(x, y)$ is periodic in x with period d_x and in y with period d_y . Since $\vec{j}_s(x, y)$ is periodic in x and y , it can be expanded in terms of a 2D Fourier series as

$$\vec{j}_s(x, y) = \sum_{p=-\infty}^{\infty} \sum_{q=-\infty}^{\infty} \bar{I}_{pq} e^{-j(k'_{xp}x + k'_{yq}y)}, \quad (22)$$

where $k'_{xp} = \frac{2\pi p}{d_x}$ and $k'_{yq} = \frac{2\pi q}{d_y}$. Substituting this into (21), we obtain

$$\vec{J}_s(x, y) = \sum_{p=-\infty}^{\infty} \sum_{q=-\infty}^{\infty} \bar{I}_{pq} e^{-j(k_{xp}x + k_{yq}y)}, \quad (23)$$

where $k_{xp} = k_{ix} + k'_{xp}$ and $k_{yq} = k_{iy} + k'_{yq}$. We can interpret (23) as an expansion of the surface current density into sheet currents with uniform amplitude \bar{I}_{pq} and a phase dependence similar to a plane wave. Therefore, at $z = 0$, the transverse scattered electric field can be written as

$$\vec{E}_{s,t}(x, y) = -jk_0 Z_0 \sum_{p=-\infty}^{\infty} \sum_{q=-\infty}^{\infty} \vec{G}(k_{xp}, k_{yq}) \bar{I}_{pq} e^{-j(k_{xp}x + k_{yq}y)}, \quad (24)$$

where $\vec{G}(k_{xp}, k_{yq})$ is the spectral-domain representation of the dyadic Green's function as derived in Appendix A. Substituting the expansion for the scattered electric field into (20) and multiplying both sides by $e^{j(k_{ix}x + k_{iy}y)}$, we obtain

$$\left[1 + \vec{\Gamma}\right] \vec{E}_{0,t} = \eta_s(x, y) \vec{j}_s(x, y) + jk_0 Z_0 \sum_{p=-\infty}^{\infty} \sum_{q=-\infty}^{\infty} \vec{G}_{pq} \bar{I}_{pq} e^{-j(k'_{xp}x + k'_{yq}y)}, \quad (25)$$

where $\vec{E}_{0,t}$ is the transverse component of the excitation field amplitude, \vec{E}_0 , and $\vec{G}_{pq} = \vec{G}(k_{xp}, k_{yq})$. As discussed in [27], (25) represents our integral equation since \bar{I}_{pq} is given by

$$\bar{I}_{pq} = \frac{1}{d_x d_y} \int_{-d_x/2}^{d_x/2} \int_{-d_y/2}^{d_y/2} \vec{j}_s(x, y) e^{j(k'_{xp}x + k'_{yq}y)} dx dy. \quad (26)$$

Numerically computing the surface current requires us to expand $\vec{j}_s(x, y)$ into a set of basis functions. Following the procedure in [27], we will expand $\vec{j}_s(x, y)$ into basis functions with finite divergence. The basis function profile for the x component of \vec{j}_s , $W_{mn}^{xx}(x, y)$, and the y component of \vec{j}_s , $W_{mn}^{yy}(x, y)$, are shown in Fig. 5. $W_{mn}^{xx}(x, y)$ is the product

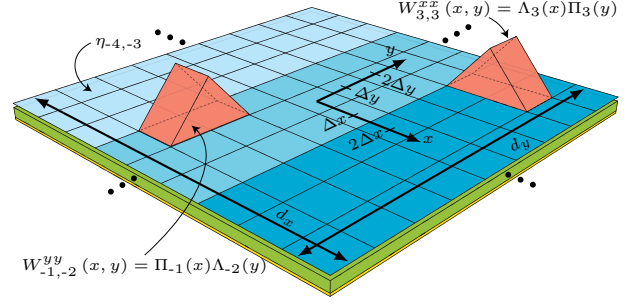


Fig. 5: An overlay of the basis functions used to expand the current within a spatial period of the structure shown in Fig. 4. In this example, there are $2M' + 1 = 9$ unknowns along x and $2N' + 1 = 9$ unknowns along y

of a rooftop function, Λ_m , in x and a pulse function, Π_n , in y . Meanwhile, $W_{mn}^{yy}(x, y)$ is the product of a rooftop function, Λ_n , in y and a pulse function, Π_m , in x .

$$W_{mn}^{xx}(x, y) = \Lambda_m(x) \Pi_n(y) \quad (27)$$

$$W_{mn}^{yy}(x, y) = \Pi_m(x) \Lambda_n(y) \quad (28)$$

The explicit form of these basis function is provided here as a reference. Assuming there are $M = 2M' + 1$ spatial unknowns along x and $N = 2N' + 1$ spatial unknowns along y ,

$$\Pi_m(x) = \begin{cases} 1, & x \in [(m - \frac{1}{2})\Delta x, (m + \frac{1}{2})\Delta x] \\ 0, & \text{otherwise} \end{cases} \quad (29)$$

$$\Pi_n(y) = \begin{cases} 1, & y \in [(n - \frac{1}{2})\Delta y, (n + \frac{1}{2})\Delta y] \\ 0, & \text{otherwise} \end{cases} \quad (30)$$

$$\Lambda_m(x) = \begin{cases} \frac{3}{2} + \frac{x}{\Delta x} - m, & x \in [(m - \frac{3}{2})\Delta x, (m - \frac{1}{2})\Delta x] \\ \frac{1}{2} - \frac{x}{\Delta x} + m, & x \in [(m - \frac{1}{2})\Delta x, (m + \frac{1}{2})\Delta x] \\ 0, & \text{otherwise} \end{cases} \quad (31)$$

$$\Lambda_n(y) = \begin{cases} \frac{3}{2} + \frac{y}{\Delta y} - n, & y \in [(n - \frac{3}{2})\Delta y, (n - \frac{1}{2})\Delta y] \\ \frac{1}{2} - \frac{y}{\Delta y} + n, & y \in [(n - \frac{1}{2})\Delta y, (n + \frac{1}{2})\Delta y] \\ 0, & \text{otherwise} \end{cases}, \quad (32)$$

where $\Delta x = d_x/M$ and $\Delta y = d_y/N$. The surface current can therefore be compactly represented as

$$\vec{j}_s(x, y) = \sum_{m'=-M'}^{M'} \sum_{n'=-N'}^{N'} \vec{W}_{m'n'}(x, y) \vec{j}_{m'n'}, \quad (33)$$

where

$$\vec{W}_{mn}(x, y) = \Lambda_m(x) \Pi_n(y) \hat{x}\hat{x} + \Pi_m(x) \Lambda_n(y) \hat{y}\hat{y}. \quad (34)$$

We can substitute (33) into (26) to obtain \bar{I}_{pq} in terms of the weighting coefficients $\vec{j}_{m'n'}$, which yields

$$\bar{I}_{pq} = \frac{1}{MN} \vec{T}_{pq} \sum_{m'n'} \vec{j}_{m'n'} e^{j(2\pi pm'/M + 2\pi qn'/N)}, \quad (35)$$

where \vec{T}_{pq} represents the 2D Fourier series coefficients of \vec{W}_{00} given by

$$\begin{aligned} \vec{T}_{pq} = & \text{sinc}^2\left(\frac{p\pi}{M}\right) \text{sinc}\left(\frac{q\pi}{N}\right) e^{j\frac{p\pi}{M}\hat{x}} \\ & + \text{sinc}\left(\frac{p\pi}{M}\right) \text{sinc}^2\left(\frac{q\pi}{N}\right) e^{j\frac{q\pi}{N}\hat{y}} \end{aligned} \quad (36)$$

We now substitute \vec{j}_s from (33) and \vec{I}_{pq} from (35) into (25) to obtain an expression relating the incident field amplitude to the unknown current weighting coefficients.

$$\begin{aligned} [1 + \vec{\Gamma}] \vec{E}_{0,t} = & \sum_{m'n'} \eta_s(x, y) \vec{W}_{m'n'}(x, y) \vec{j}_{m'n'} \\ & + j \frac{k_0 Z_0}{MN} \sum_{m'n'} \sum_{pq} e^{-j(k'_{xp}x + k'_{yq}y)} \vec{G}_{pq} \vec{T}_{pq} H_{m'n'}^{pq} \vec{j}_{m'n'} \end{aligned}, \quad (37)$$

where $H_{m'n'}^{pq} = e^{j(2\pi pm'/M + 2\pi qn'/N)}$ is the phase term from (35).

The final MoM matrix equation can be obtained by testing the left- and right-hand sides of (37) with

$$\begin{aligned} \frac{1}{d_x d_y} \int_{-d_x/2}^{d_x/2} \int_{-d_y/2}^{d_y/2} \vec{W}_{mn}(x, y) \{\bullet\} dx dy \\ \forall \{m \in [-M', M'], n \in [-N', N']\}. \end{aligned} \quad (38)$$

Here, we have chosen to use the Galerkin method, i.e., the testing functions are the same as the basis functions. The testing operation is carried out for all observation positions $(m\Delta x, n\Delta y)$ within the spatial period. To obtain an explicit form for the entries of the MoM matrix, we will approximate the surface impedance as a summation over pulse functions.

$$\eta_s(x, y) = \sum_{m''=-M'}^{M'} \sum_{n''=-N'}^{N'} \Pi_{m''}(x) \Pi_{n''}(y) \eta_{m''n''} \quad (39)$$

Carrying out the integrations, we obtain the final MoM matrix equation, which can be written as

$$\begin{aligned} [1 + \vec{\Gamma}] \vec{E}_{0,t} = & \sum_{m'n'} \left(\vec{\eta}_{mn, m'n'} + \vec{Z}_{m-m', n-n'} \right) \vec{j}_{m'n'} \\ & \forall \{m \in [-M', M'], n \in [-N', N']\} \end{aligned}, \quad (40)$$

where

$$\begin{aligned} \hat{x} \cdot \vec{\eta}_{mn, m'n'} \cdot \hat{x} = \\ \delta_{n-n'} \begin{cases} \frac{1}{6} \eta_{m-1, n}, & m' = m - 1 \\ \frac{1}{3} \{ \eta_{m-1, n} + \eta_{m, n} \}, & m' = m \\ \frac{1}{6} \eta_{m, n}, & m' = m + 1 \\ 0, & \text{otherwise} \end{cases} \end{aligned} \quad (41)$$

$$\begin{aligned} \hat{y} \cdot \vec{\eta}_{mn, m'n'} \cdot \hat{y} = \\ \delta_{m-m'} \begin{cases} \frac{1}{6} \eta_{m, n-1}, & n' = n - 1 \\ \frac{1}{3} \{ \eta_{m, n-1} + \eta_{m, n} \}, & n' = n \\ \frac{1}{6} \eta_{m, n}, & n' = n + 1 \\ 0, & \text{otherwise} \end{cases} \end{aligned} \quad (42)$$

$$\hat{x} \cdot \vec{\eta}_{mn, m'n'} \cdot \hat{y} = \hat{y} \cdot \vec{\eta}_{mn, m'n'} \cdot \hat{x} = 0 \quad (43)$$

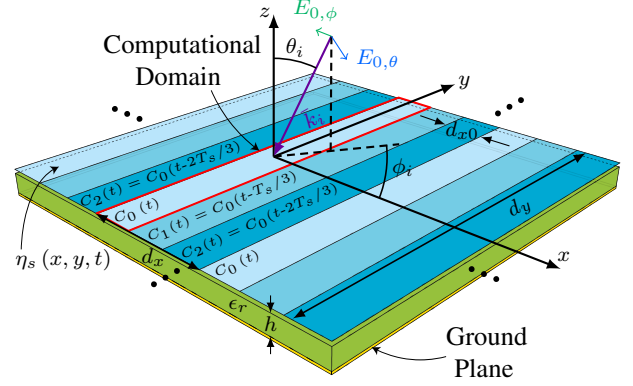


Fig. 6: An example of a 3-stixel SD-TWM structure examined in [1]. Since there are 3 stixels per supercell ($L = 3$) the time-dependence of the capacitance in stixel l is given by $C_l(t) = C_0(t - \frac{l}{L}T_s) = C_0(t - \frac{l}{3}T_s)$. The width of each stixel is $d_{x0} = d_x/L = d_x/3$. The presented formulation is valid for periodic variations along y , although this is not depicted in the figure.

$$\vec{Z}_{\Delta m, \Delta n} = j \frac{k_0 Z_0}{MN} \sum_{pq} \vec{T}_{pq}^* \vec{G}_{pq} \vec{T}_{pq} e^{-j2\pi(\frac{p\Delta m}{M} + \frac{q\Delta n}{N})}. \quad (44)$$

In summary, (40) is the MoM matrix equation corresponding to the structure shown in Fig. 4. Using Floquet's theorem, the periodicity in space was exploited such that unknowns only had to be placed within a single spatial period. For each observation position $(m\Delta x, n\Delta y)$ within a spatial period, $\vec{\eta}_{mn, m'n'}$ represents the overlap integral between the testing function at the observation position, the surface impedance distribution and the basis functions. Since the system is linear and time-invariant (LTI), this term contains no interactions between fields of different frequencies. Meanwhile, the interactions due to the surrounding medium are captured by the matrix $\vec{Z}_{m-m', n-n'}$. Since the surrounding medium is LTI, this term also does not contain any interactions between fields of different frequencies.

B. Spatially-Discrete Traveling-Wave Modulated Structure

In this section, the MoM formulation for the SD-TWM structure shown in Fig. 6 will be derived. However, it should be noted that the following procedure can easily be extended to simulate other SD-TWM structures. The MoM formulation will be obtained by modifying the time-invariant analysis in Section III-A to account for a SD-TWM impedance sheet. The interpath relation in (12) will be used to construct basis functions such that unknowns will only need to be placed within a single stixel. Therefore, the following analysis procedure reduces the number of unknowns by a factor of L , the number of stixels in a supercell.

The structure in Fig. 6 consists of time-varying capacitive strips placed on the surface of a grounded dielectric substrate. The time variation of the capacitance within each stixel is staggered in time. That is, the sheet capacitance in stixel l , $C_l(t)$, satisfies

$$C_l(t) = C_{l-1}(t - T_s/L), \quad (45)$$

where L is the number of stixels in a supercell. The space-time dependent sheet capacitance over the entire supercell can then be written

$$C(x, t) = C_l(t), \quad x \in \left[\left(l - \frac{1}{2}\right) d_{x0}, \left(l + \frac{1}{2}\right) d_{x0} \right]. \quad (46)$$

The excitation field is the same as in Section III-A, and can be written in the time-domain as

$$\begin{aligned} \bar{\mathcal{E}}_i(\bar{r}, t) &= \bar{E}_0 e^{j(\omega_0 t - \bar{k}_i \cdot \bar{r})} \\ &= \bar{E}_i(\bar{r}) e^{j\omega_0 t} \end{aligned} \quad (47)$$

Similar to the time-invariant formulation, we will first write the boundary condition for the total field at $z = 0$. For a sheet capacitance, this boundary condition is given by

$$\frac{\partial}{\partial t} \{C(x, t) \bar{\mathcal{E}}_t(x, y, t)\} = \bar{\mathcal{J}}_s(x, y, t), \quad (48)$$

where $\bar{\mathcal{E}}_t(x, y, t)$ denotes the transverse component of the total time-dependent electric field. However, for our formulation, it is simpler to implement the following, equivalent boundary condition

$$\begin{aligned} \bar{\mathcal{E}}_t(x, y, t) &= \frac{1}{C(x, t)} \int \bar{\mathcal{J}}_s(x, y, t) dt \\ &= \frac{j\omega_0}{j\omega_0 C(x, t)} \int \bar{\mathcal{J}}_s(x, y, t) dt, \quad (49) \\ &= \eta_s(x, y, t) j\omega_0 \int \bar{\mathcal{J}}_s(x, y, t) dt \end{aligned}$$

where $\eta_s(x, y, t) \triangleq 1/j\omega_0 C(x, t)$ is the effective time-varying surface impedance. Since $C(x, t)$ is a periodic function in time, $\eta_s(x, y, t)$ is also periodic, and can be expanded in a Fourier series as

$$\eta_s(x, y, t) = \sum_{\nu=-\infty}^{\infty} \eta_s^\nu(x, y) e^{j\nu\omega_s t}. \quad (50)$$

Further, since the excitation field in (47) has a time-dependence of $e^{j\omega_0 t}$ and the structure is an LPTV system, the electric field and surface current density can be written as [24]

$$\begin{aligned} \bar{\mathcal{E}}_t(x, y, t) &= \sum_{\nu=-\infty}^{\infty} \bar{E}_t^\nu(x, y) e^{j(\omega_0 + \nu\omega_s)t} \\ \bar{\mathcal{J}}_s(x, y, t) &= \sum_{\nu'=-\infty}^{\infty} \bar{J}_s^{\nu'}(x, y) e^{j(\omega_0 + \nu'\omega_s)t} \end{aligned} \quad (51)$$

Note that this implies

$$j\omega_0 \int \bar{\mathcal{J}}_s(x, y, t) dt = \sum_{\nu'=-\infty}^{\infty} \frac{\bar{J}_s^{\nu'}(x, y)}{1 + \nu'\frac{\omega_s}{\omega_0}} e^{j(\omega_0 + \nu'\omega_s)t}. \quad (52)$$

Substituting this expression into (49) yields

$$\bar{E}_t^\nu(x, y) = \sum_{\nu'=-\infty}^{\infty} \frac{\eta_s^{\nu-\nu'}(x, y)}{1 + \nu'\frac{\omega_s}{\omega_0}} \bar{J}_s^{\nu'}(x, y). \quad (53)$$

This is expected since a product in the time-domain results in convolution in the frequency-domain. Equation (53) is the boundary condition we will use in the MoM formulation. Note the similarity between this expression and (18). In effect, (53) will yield an integral equation for each ‘‘observed’’ frequency

harmonic, ν , which is coupled to all ‘‘source’’ frequency harmonics, ν' , through the surface impedance. We will now split the total electric field harmonics into incident and scattered components. The electric field in the absence of the space-time modulated impedance sheet contains both the excitation field as well as the reflected field from the grounded dielectric. In the time-domain, the reflected field is given by

$$\bar{\mathcal{E}}_{r,t}(x, y, t) = \overleftrightarrow{\Gamma} \bar{\mathcal{E}}_{i,t}(x, y, t), \quad (54)$$

where $\overleftrightarrow{\Gamma}$ is the dyadic reflection coefficient which is a function of θ_i , ϕ_i , h and ϵ_r . Splitting the total field in (53) into incident and scattered components, we obtain

$$\begin{aligned} [1 + \overleftrightarrow{\Gamma}] \bar{E}_{i,t}(x, y) \delta_\nu + \bar{E}_{s,t}^\nu(x, y) \\ = \sum_{\nu'=-\infty}^{\infty} \frac{\eta_s^{\nu-\nu'}(x, y)}{1 + \nu'\frac{\omega_s}{\omega_0}} \bar{J}_s^{\nu'}(x, y), \end{aligned} \quad (55)$$

where $\bar{E}_{i,t}(x, y)$ is the transverse component of $\bar{E}_i(\bar{r})$ in (47) and $\bar{E}_{s,t}^\nu(x, y)$ is the transverse component of the ν^{th} frequency harmonic of the scattered electric field. The Kronecker delta function which multiplies the incident field in (55) results from the monochromatic excitation.

We will now express the scattered electric field frequency harmonics in terms of the surface current density. Because the surrounding medium is time-invariant (only the surface impedance is time-dependent), the scattered field at frequency $f_0 + \nu f_s$ only depends on the induced current at the same frequency. Since the supercell is periodic in x and y , it follows from Floquet’s theorem that

$$\bar{J}_s^\nu(x, y) = e^{-j(k_{ix}x + k_{iy}y)} \bar{j}_s^\nu(x, y), \quad (56)$$

where $\bar{j}_s^\nu(x, y)$ is a periodic function in x with period d_x and in y with period d_y . Since $\bar{j}_s^\nu(x, y)$ is periodic in x and y , it can be expanded in terms of 2D Fourier series as

$$\bar{j}_s^\nu(x, y) = \sum_{p=-\infty}^{\infty} \sum_{q=-\infty}^{\infty} \bar{I}_{pq}^\nu e^{-j(k'_{xp}x + k'_{yq}y)}, \quad (57)$$

where $k'_{xp} = \frac{2\pi p}{d_x}$ and $k'_{yq} = \frac{2\pi q}{d_y}$. Substituting this into (56), we obtain

$$\bar{J}_s^\nu(x, y) = \sum_{p=-\infty}^{\infty} \sum_{q=-\infty}^{\infty} \bar{I}_{pq}^\nu e^{-j(k_{xp}x + k_{yq}y)}, \quad (58)$$

where $k_{xp} = k_{ix} + k'_{xp}$ and $k_{yq} = k_{iy} + k'_{yq}$. Just as in Section III-A, we can interpret (58) as a superposition of planar current sheets of the form $\bar{J}_0 e^{-j(k_x x + k_y y)}$. Therefore, the electric field scattered by the surface current density can be written as [27]

$$\begin{aligned} \bar{E}_{s,t}^\nu(x, y) &= \\ &-jk_0 Z_0 \sum_{p=-\infty}^{\infty} \sum_{q=-\infty}^{\infty} \overleftrightarrow{G}^\nu(k_{xp}, k_{yq}) \bar{I}_{pq}^\nu e^{-j(k_{xp}x + k_{yq}y)}, \end{aligned} \quad (59)$$

where $\overleftrightarrow{G}^\nu(k_{xp}, k_{yq})$ is the spectral-domain representation of the dyadic Green’s function as derived in Appendix A evaluated at frequency $f_0 + \nu f_s$. Substituting the expansion for the

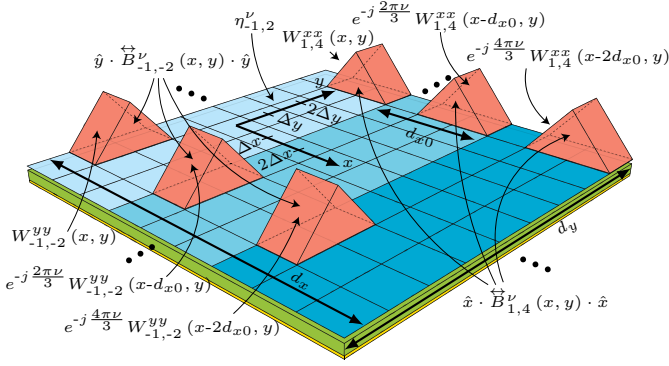


Fig. 7: An overlay of the basis functions used to expand the current within a supercell of the structure shown in Fig. 6. In this example, there are 3 stixels within a supercell ($d_x = 3d_{x0}$). There are only $2M' + 1 = 3$ unique unknowns along x since the basis functions account for the interpath relation, reducing the number of unknowns with respect to Fig. 5. There are $2N' + 1 = 9$ unknowns along y

scattered electric field into (55) and multiplying both sides by $e^{j(k_{ix}x + k_{iy}y)}$, we obtain

$$\begin{aligned} [1 + \vec{\Gamma}] \vec{E}_{0,t} \delta_\nu &= \sum_{\nu'=-\infty}^{\infty} \frac{\eta_s^{\nu-\nu'}(x,y) \bar{j}_s^{\nu'}(x,y)}{1 + \nu' \frac{\omega_s}{\omega_0}} \\ &+ jk_0 Z_0 \sum_{p=-\infty}^{\infty} \sum_{q=-\infty}^{\infty} \vec{G}_{pq}^{\nu} \bar{I}_{pq}^{\nu} e^{-j(k'_{xp}x + k'_{yq}y)}, \end{aligned} \quad (60)$$

where $\vec{E}_{0,t}$ is the transverse component of the excitation field amplitude and $\vec{G}_{pq}^{\nu} = \vec{G}^{\nu}(k_{xp}, k_{yq})$. Equation (60) represents our integral equation since \bar{I}_{pq}^{ν} is computed via a spatial integral over the supercell

$$\bar{I}_{pq}^{\nu} = \frac{1}{d_x d_y} \int_{-\frac{d_{x0}}{2}}^{\frac{d_{x0}}{2}} \int_{-\frac{d_y}{2}}^{\frac{d_y}{2}} \bar{j}_s^{\nu}(x,y) e^{j(k'_{xp}x + k'_{yq}y)} dx dy. \quad (61)$$

Numerically computing the current requires us to expand $\bar{j}_s^{\nu}(x,y)$ into a set of basis functions. It should be noted that, up to this point, we have not invoked the symmetry of the SD-TWM structure. In fact, using the same basis functions as those described in Section III-A would result in the standard harmonic-balance MoM approach to solving the structure in Fig. 6. However, from the interpath relation in (12), it is clear that the fields in a single stixel should be sufficient to solve the entire problem. Thus, to reduce the number of unknowns required to simulate the structure, we will modify the basis functions applied to the time-invariant problem in Section III-A. The modified basis will be constructed such that:

- surface current weighting coefficients only need to be placed within a single stixel
- the modified basis functions satisfy the interpath relation in (12)

We will define $\vec{W}_{mn}(x,y)$ to be the same as in (27) through (32). However, in this section, we require the computational grid to be identical within each stixel. Therefore, we redefine

M as the number of computational elements within a stixel (rather than a spatial period). This re-scales the width of the computational elements to be $\Delta x = d_{x0}/M$ rather than d_x/M . We will now construct a new basis function $\vec{B}_{m'n'}^{\nu}(x,y)$, shown in Fig. 7, which is given by

$$\vec{B}_{m'n'}^{\nu}(x,y) = \sum_{l=0}^{L-1} e^{-j \frac{2\pi\nu l}{L}} \vec{W}_{m'n'}^{\nu}(x - ld_{x0}, y). \quad (62)$$

Note that $\vec{B}_{m'n'}^{\nu}(x,y)$ satisfies the interpath relation in (12) and spans the entire supercell. The expansion of $\bar{j}_s^{\nu}(x,y)$ in terms of basis functions $\vec{B}_{m'n'}^{\nu}(x,y)$ is given by

$$\bar{j}_s^{\nu}(x,y) = \sum_{n=-N'}^{N'} \sum_{m=-M'}^{M'} \vec{B}_{m'n'}^{\nu}(x,y) \bar{j}_{m'n'}^{\nu}. \quad (63)$$

We can substitute this expansion into (61) to obtain \bar{I}_{pq}^{ν} in terms of the weighting coefficients $\bar{j}_{m'n'}^{\nu}$, which yields

$$\begin{aligned} \bar{I}_{pq}^{\nu} &= \\ &\frac{\vec{T}_{pq}}{LMN} \sum_{m'n'} \sum_{l=0}^{L-1} e^{j \frac{2\pi(p-\nu)l}{L}} \bar{j}_{m'n'}^{\nu} e^{j \left(\frac{2\pi pm'}{LM} + \frac{2\pi qn'}{N} \right)}, \end{aligned} \quad (64)$$

where \vec{T}_{pq} represents the 2D Fourier series coefficients of \vec{W}_{00}^{ν} given by

$$\begin{aligned} \vec{T}_{pq} &= \text{sinc}^2 \left(\frac{p\pi}{LM} \right) \text{sinc} \left(\frac{q\pi}{N} \right) e^{j \frac{p\pi}{LM} \hat{x}\hat{x}} \\ &+ \text{sinc} \left(\frac{p\pi}{LM} \right) \text{sinc}^2 \left(\frac{q\pi}{N} \right) e^{j \frac{q\pi}{N} \hat{y}\hat{y}}. \end{aligned} \quad (65)$$

The factor of $1/L$ in (64) and (65) results from an effective increase in discretization by a factor of L . This expression can be further simplified by noting

$$\sum_{l=0}^{L-1} e^{j \frac{2\pi(p-\nu)l}{L}} = \begin{cases} L, & p - \nu = p'L, p' \in \mathbb{Z} \\ 0, & \text{otherwise} \end{cases}. \quad (66)$$

If we define

$$g_p^{\nu} = \begin{cases} 1, & p - \nu = p'L, p' \in \mathbb{Z} \\ 0, & \text{otherwise} \end{cases}, \quad (67)$$

then the summation over l (the stixels) in (64) can be eliminated. Thus (64) can be written as

$$\bar{I}_{pq}^{\nu} = \frac{\vec{T}_{pq}}{MN} \sum_{m'n'} g_p^{\nu} \bar{j}_{m'n'}^{\nu} e^{j(2\pi pm'/LM + 2\pi qn'/N)}. \quad (68)$$

We now substitute \bar{j}_s^{ν} from (63) and \bar{I}_{pq}^{ν} from (68) into (60) to obtain an expression relating the incident field amplitude to the unknown current weighting coefficients.

$$\begin{aligned} [1 + \vec{\Gamma}] \vec{E}_{0,t} \delta_\nu &= \sum_{\nu'} \sum_{m'n'} \frac{\eta_s^{\nu-\nu'}(x,y)}{1 + \nu' \frac{\omega_s}{\omega_0}} \vec{B}_{m'n'}^{\nu'}(x,y) \bar{j}_{m'n'}^{\nu'} \\ &+ j \frac{k_0 Z_0}{MN} \sum_{m'n'} \sum_{pq} e^{-j(k'_{xp}x + k'_{yq}y)} g_p^{\nu} \vec{G}_{pq}^{\nu} \vec{T}_{pq} H_{m'n'}^{pq} \bar{j}_{m'n'}^{\nu}, \end{aligned} \quad (69)$$

where $H_{m'n'}^{pq} = e^{j(2\pi pm'/LM + 2\pi qn'/N)}$ is the phase term from (68). It is worth noting the similarity between this

expression and (37). The first term on the right-hand side of (69) now includes a summation over source frequencies $f_0 + \nu' f_s$, representing the coupling between frequencies introduced by the time-varying impedance sheet. Meanwhile, the only difference in the second term of these two equations is the factor g_p^ν which captures the induced tangential momentum imparted by the SD-TWM.

The final MoM matrix equation can be obtained by testing the left- and right-hand sides of (69) for observation points within a single stixel

$$\frac{1}{d_x d_y} \int_{-\frac{d_x}{2}}^{\frac{d_x}{2}} \int_{-\frac{d_y}{2}}^{\frac{d_y}{2}} \overleftrightarrow{W}_{mn}(x, y) \{\bullet\} dx dy \quad \forall \{m \in [-M', M'], n \in [-N', N']\}. \quad (70)$$

Note that, while the integral bounds span the entire supercell, the observation positions $(m\Delta x, n\Delta y)$ are limited to a single stixel. For this implementation, we will approximate the surface impedance frequency harmonics as summations over pulse functions.

$$\eta_s^\nu(x, y) = \sum_{m'=-M'}^{M'} \sum_{n'=-N'}^{N'} \Pi_{m'}(x) \Pi_{n'}(y) \eta_{m'n'}^\nu \quad (71)$$

Carrying out the integrations, we obtain the final MoM matrix equation, which can be written as

$$\left[1 + \overleftrightarrow{\Gamma}\right] \overleftrightarrow{E}_{0,t} \delta_\nu = \sum_{\nu'} \sum_{m'n'} \left(\frac{\overleftrightarrow{\eta}_{mn,m'n'}^{\nu-\nu'}}{1 + \nu' \frac{\omega_s}{\omega_0}} + \overleftrightarrow{Z}_{m-m', n-n'}^{\nu'} \delta_{\nu-\nu'} \right) \overleftrightarrow{j}_{m'n'}^{\nu'} \quad \forall \{m \in [-M', M'], n \in [-N', N']\}, \quad (72)$$

where

$$\hat{x} \cdot \overleftrightarrow{\eta}_{mn,m'n'}^\nu \cdot \hat{x} = \delta_{n-n'} \begin{cases} \frac{1}{6} \eta_{m-1,n}^\nu, & m' = m-1 \\ \frac{1}{3} \{ \eta_{m-1,n}^\nu + \eta_{m,n}^\nu \}, & m' = m \\ \frac{1}{6} \eta_{m,n}^\nu, & m' = m+1 \\ 0, & \text{otherwise} \end{cases} \quad (73)$$

$$\hat{y} \cdot \overleftrightarrow{\eta}_{mn,m'n'}^\nu \cdot \hat{y} = \delta_{m-m'} \begin{cases} \frac{1}{6} \eta_{m,n-1}^\nu, & n' = n-1 \\ \frac{1}{3} \{ \eta_{m,n-1}^\nu + \eta_{m,n}^\nu \}, & n' = n \\ \frac{1}{6} \eta_{m,n}^\nu, & n' = n+1 \\ 0, & \text{otherwise} \end{cases} \quad (74)$$

$$\hat{x} \cdot \overleftrightarrow{\eta}_{mn,m'n'}^\nu \cdot \hat{y} = \hat{y} \cdot \overleftrightarrow{\eta}_{mn,m'n'}^\nu \cdot \hat{x} = 0, \quad (75)$$

and

$$\begin{aligned} \overleftrightarrow{Z}_{\Delta m, \Delta n}^\nu &= j \frac{k_0 Z_0}{MN} \sum_{pq} g_p^\nu \overleftrightarrow{T}_{pq}^* \overleftrightarrow{G}_{pq}^\nu \overleftrightarrow{T}_{pq} e^{-j2\pi \left(\frac{p\Delta m}{LM} + \frac{q\Delta n}{N} \right)} \\ &= j \frac{k_0 Z_0}{MN} e^{-j \frac{2\pi\nu\Delta m}{LM}} \sum_{p'q} \overleftrightarrow{F}_{p'q}^\nu e^{-j2\pi \left(\frac{p'\Delta m}{M} + \frac{q\Delta n}{N} \right)} \end{aligned} \quad (76)$$

$$\overleftrightarrow{F}_{p'q}^\nu = \overleftrightarrow{T}_{p'L+\nu_e, q}^* \overleftrightarrow{G}_{p'L+\nu_e, q}^\nu \overleftrightarrow{T}_{p'L+\nu_e, q} \quad (77)$$

$$\nu_e = \text{mod}(\nu, L). \quad (78)$$

In summary, (72) represents the MoM matrix equation corresponding to the structure shown in Fig. 6. Due to the interpath relation, unknowns only need to be placed within a single stixel (as opposed to the entire supercell). For each observed frequency ν and position $(m\Delta x, n\Delta y)$ within a single stixel, $\overleftrightarrow{\eta}_{mn,m'n'}^{\nu-\nu'}$ represents the overlap integral between the testing function at the observation position, the spatial distribution of frequency harmonic $\nu - \nu'$ of the effective time-varying surface impedance, and the basis functions corresponding to frequency ν' . Since the surface impedance is LPTV, this term captures the interactions between fields of different frequencies. Meanwhile, the interactions due to the surrounding medium are captured by the matrix $\overleftrightarrow{Z}_{m-m', n-n'}^{\nu'}$. Since the surrounding medium is LTI, this term is only included when the observed frequency is equal to the source frequency (as denoted by $\delta_{\nu-\nu'}$).

The interpath relation serves to reduce the required number of unknowns in the MoM matrix equation. It is clear that, without invoking the interpath relation, the number of unknowns would have scaled as $\mathcal{O}(UNLM)$, where

- U - number of simulated frequency harmonics
- N - number of unknowns along y within a spatial period
- L - number of stixels per supercell
- M - number of unknowns along x within a single stixel.

By including the interpath relation, the number of unknowns scales as $\mathcal{O}(UNM)$, reducing the problem size by a factor of L . As discussed in [1], structures built to mimic continuous traveling-wave modulation require an appreciable number of stixels per spatial modulation period. In these scenarios, the reduction in unknowns which results from shrinking the computational domain to a single stixel would be particularly significant.

IV. NUMERICAL SIMULATION RESULTS

In this section, numerical results of the MoM formulation presented in Section III-B for the structure shown in Fig. 6 are validated and discussed. In [1], various capabilities are achieved by considering the metasurface in Fig. 6 as a space-time reflection phase modulator. Consider a uniform sheet capacitance, C , placed on top of a grounded dielectric. For a given polarization and incidence angle, it can be shown that the reflection phase, ϕ , satisfies [1]

$$\tan \frac{\phi^{\text{TX}}}{2} = -Z_0^{\text{TX}} \omega_0 C_0^{\text{TX}} \Delta C, \quad (79)$$

where the superscript TX refers to either TE_z or TM_z polarization, Z_0^{TX} is the tangential wave impedance in free space, ω_0 is RF frequency, C_0^{TX} is the resonant value of

TABLE I: Summary of modulation examples studied in Section IV.

	Case		
	A	B	C
RF Carrier Frequency (f_0)	10 GHz	10 GHz	10 GHz
Incident Angle (θ_i)	25°	25°	25°
Modulation Frequency (f_s)	25 kHz	25 kHz	500 MHz
Stixel Width (d_{x0})	$\lambda_0/5$	$\lambda_0/5$	$\lambda_0/10$
Dielectric Thickness (h)	0.508 mm	0.508 mm	0.508 mm
Stixels per Supercell (L)	20	3	60
Capacitance Waveform	sawtooth phase	sawtooth phase	sinusoidal

capacitance for each polarization, and Δ_C is defined such that $C = C_0^{\text{TX}}(1 + \Delta_C)$. Therefore, given a desired phase variation, (79) can be used to find the required capacitance variation.

Three modulation examples of the structure shown in Fig. 6 are examined within this section. Note that, for all examples, the capacitance is assumed to be spatially uniform over each stixel. Further, \vec{k}_i is assumed to be in the x - z plane ($k_{iy} = 0$). The problem descriptions for each of the three modulations are summarized in Table I. In Section IV-A, the time-variation of the capacitance is designed to produce a sawtooth reflection phase. There are 20 stixels of width $\lambda_0/5$ per supercell. The convergence of the MoM formulation is examined, and the results are validated using a spectral-domain method [1]. In Section IV-B, the capacitance variation again produces a sawtooth reflection phase. However, in this case, each supercell contains only 3 stixels (becoming subwavelength) and subharmonic mixing can be observed. Finally, in Section IV-C, a sinusoidal capacitance is applied such that the reflected field contains no power at the fundamental frequency or in the spectral direction. In this example, each supercell contains 60 stixels of width $\lambda_0/10$, highlighting the capability of the MoM formulation to efficiently simulate continuous designs.

To examine the accuracy and convergence of the proposed method, we will define the error energy between two given solutions in the spectral-domain. From the interpath relation, it can be shown that the fields corresponding to a SD-TWM structure are written in terms of a compressed double Floquet expansion [1]. Assuming that there is no variation along y , the transverse component of the scattered electric field at $z = 0$ can be expanded as [1]

$$\bar{\mathcal{E}}_{s,t}(x, y, t) = e^{j(\omega_0 t - k_{ix} x)} \sum_{p'=-\infty}^{\infty} \sum_{\nu=-\infty}^{\infty} \bar{E}_{p'}^{\nu} e^{j\nu(\omega_s t - \frac{2\pi}{d_x} x)} e^{-j\frac{2\pi p'}{d_{x0}} x}. \quad (80)$$

This is the expansion employed in the spectral-domain method reported in [1] that will be used to determine the accuracy of the MoM formulation. From the weighting coefficients,

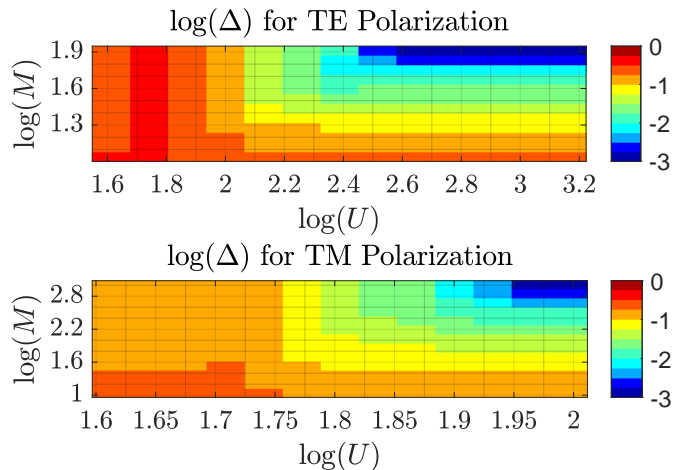


Fig. 8: Error energy defined in (81) in the electric field harmonic coefficients computed by the MoM solver compared to the finest solution. The number of frequency harmonics is denoted by U while the number of spatial samples is denoted by M .

$\bar{j}_{m'n'}^{\nu}$, computed by the MoM solver, the spectral expansion of the field can be obtained in this form using (68) and (59). Thus, given two solutions for the spectral-domain electric field coefficients, $\bar{E}_{p'}^{\nu(1)}$ and $\bar{E}_{p'}^{\nu(2)}$, we define the error energy as

$$\Delta(\bar{E}^{(1)}, \bar{E}^{(2)}) = \sqrt{\frac{\sum_{\nu=-U'}^{U'} \sum_{p'=-P'}^{P'} \left| \bar{E}_{p'}^{\nu(1)} - \bar{E}_{p'}^{\nu(2)} \right|^2}{\sum_{\nu=-U'}^{U'} \sum_{p'=-P'}^{P'} \left| \bar{E}_{p'}^{\nu(2)} \right|^2}}. \quad (81)$$

Throughout this section, the summations in (81) are truncated such that $U' = P' = 30$.

A. Validation and Convergence Study

Here, the convergence and accuracy of the solution obtained by the MoM formulation is examined when the metasurface is modulated as described in case A of Table I. The size of each supercell is given by $d_x = Ld_{x0} = 4\lambda_0$. In this limit, the sawtooth phase modulation waveform results in a Blaze grating [28] in both space and time. As a result, we expect the reflected power to be up-converted in frequency and deflected away from the specular direction. The convergence is studied by computing the error energy in (81) between the solution for a given number of spatial/spectral unknowns and the solution using the most spatial/spectral unknowns. The accuracy of the formulation is determined by the error energy between the spectral-domain method reported in [1] and the presented MoM formulation using the most spatial/spectral unknowns.

For a given number of spatial unknowns, M , and spectral unknowns, U , we define $\bar{E}^{(M,U)}$ as the spectral coefficients obtained from the MoM solver. We can then define the error energy in (81) with respect to discretization as $\Delta(\bar{E}^{(M,U)}, \bar{E}^{(M_0,U_0)})$, where M_0 and U_0 are the maximum simulated values of M and U in the convergence study. The

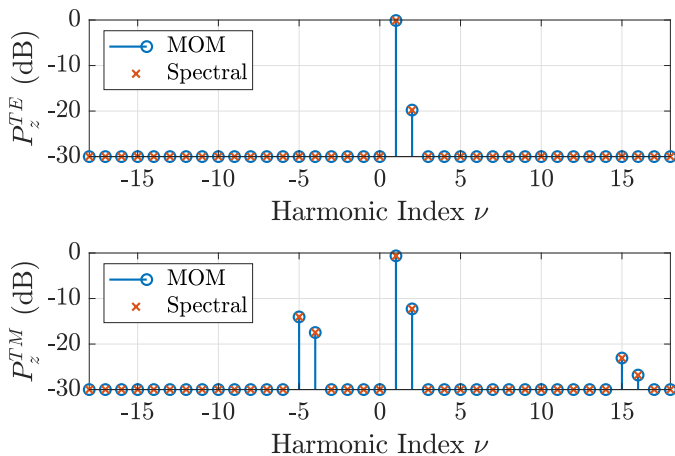


Fig. 9: Normal power radiated at each frequency $f_0 + \nu f_s$ from the metasurface in Fig. 6 modulated as specified in case A of Table I. In this case, the metasurface up-converts and deflects the scattered field. It can be seen that the MoM solver and spectral-domain methods are in good agreement.

solutions for TE_z and TM_z illumination require different numbers of spatial and spectral unknowns to converge. For the TE_z convergence study, $M_0 = 81$ and $U_0 = 1,441$. Meanwhile, for the TM_z convergence study, $M_0 = 999$ and $U_0 = 99$. In Fig. 8, the error energy is shown as a function of M and U for both polarizations. For TE_z polarization, $M = 55$ spatial samples and $U = 323$ frequency harmonics were required to reduce the error energy below 0.01. Meanwhile, for TM_z polarization, $M = 465$ spatial samples and $U = 79$ frequency harmonics were required to reduce the error energy below 0.01. The large number of required unknowns highlights the importance of using the interpath relation to solve SD-TWM systems. For example, the total number of unknowns needed for the TE_z case is $2 \times 55 \times 323 \approx 36 \times 10^3$. Without including the interpath relation, the total number of unknowns would have been $20 \times 2 \times 55 \times 323 \approx 711 \times 10^3$. Despite taking advantage of the inherent sparsity of the matrix system, it would require about 36 GB just to store such a matrix with floating point accuracy. Meanwhile, the interpath relation reduces this requirement to 0.61 GB.

The spectrum computed by the spectral-domain method as well as the finest MoM solution is shown in Fig. 9. As expected, the sawtooth wave up-converts the scattered wave to $f_0 + f_s$ and deflects it to 42.3° . The expansion in (80) used by the spectral-domain method was truncated at $p' = \pm 40$ and $\nu = \pm 720$ for TE illumination and at $p' = \pm 100$ and $\nu = \pm 49$ for TM illumination. The error energy between the spectral-domain method and the MoM solver is $\Delta(\bar{E}^{(MoM)}, \bar{E}^{(Spec)}) = 4.2 \times 10^{-3}$ for the TE_z simulation and $\Delta(\bar{E}^{(MoM)}, \bar{E}^{(Spec)}) = 5.0 \times 10^{-3}$ for the TM_z simulation, confirming the validity of the MoM solver.

B. Subwavelength Modulation Period

In this example, results of the MoM and spectral-domain solvers will be compared for the metasurface modulation described in case B of Table I. The only difference between

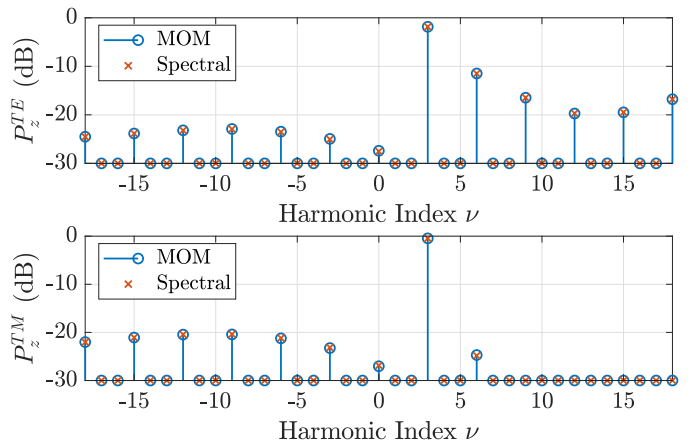


Fig. 10: Normal power radiated at each frequency $f_0 + \nu f_s$ from the metasurface in Fig. 6 modulated as specified in case B of Table I. In this case, the metasurface up-converts the scattered field to a higher-order harmonic of the modulation (sub-harmonic mixing). This behavior does not arise in the continuous model of traveling-wave modulation.

cases A and B is that the number of stixels per supercell is reduced from 20 to 3. Since the stixel size remains the same, this reduces the supercell size from $4\lambda_0$ to $0.6\lambda_0$. As a result, propagation is only supported for frequencies $f_0 + p \times 3f_s$ for $p \in \mathbb{Z}$. Thus, when a sawtooth phase modulation waveform is applied to the metasurface, we expect the reflected signal to be up-converted from f_0 to $f_0 + 3f_s$ [1]. This result is confirmed in Fig. 10. A snapshot of the spatial profile of the scattered electric field for the TE_z case is shown in Fig. 11. Since the modulation frequency is small with respect to the RF carrier frequency ($f_s/f_0 = 2.5 \times 10^{-6}$), all the reflected energy is directed in the specular direction. In the MoM simulation, the current expansion included $M = 301$ spatial samples and $U = 601$ frequency harmonics. The expansion in (80) used by the spectral-domain method was truncated at $p' = \pm 50$ and $\nu = \pm 300$. The error energy between the MoM and spectral-domain solvers is $\Delta(\bar{E}^{(MoM)}, \bar{E}^{(Spec)}) = 9.9 \times 10^{-4}$ for TE_z polarization and $\Delta(\bar{E}^{(MoM)}, \bar{E}^{(Spec)}) = 8.7 \times 10^{-3}$ for TM_z polarization.

C. Continuum Limit - Sinusoidal Traveling-Wave

As a final example, we consider a nearly continuous structure described by case C of Table I. In this case, there are 60 stixels included in a spatial period, and the stixel size is brought down to $\lambda_0/10$ (thus the supercell size is $6\lambda_0$). Additionally, we assume that the sheet capacitance is sinusoidally modulated at a frequency of 500 MHz. For a spatially uniform sheet capacitance, we observe from (79) that the ν^{th} Fourier series coefficient of the reflection coefficient, Γ_ν , can be computed as

$$\Gamma_\nu = \frac{1}{T_s} \int_{t=0}^{T_s} e^{-2j t \tan^{-1}(Z_0^{\text{TX}} \omega_0 C_0^{\text{TX}} \Delta_C(t))} e^{-j\nu \omega_s t} dt. \quad (82)$$

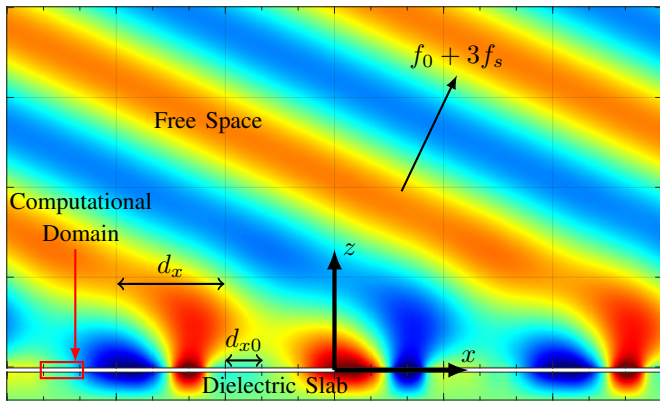


Fig. 11: Time snapshot of the scattered electric field profile for the metasurface in Fig. 6 modulated as described in case B of Table I for TE_z incidence ($\bar{E} = E_y \hat{y}$). Note that the two regions are not drawn to scale. The scattered plane wave at the up-converted frequency $f_0 + 3f_s$ can be seen propagating away from the metasurface into free space.

Thus, if $Z_0^{TX} \omega_0 C_0^{TX} \Delta_C(t) = A \cos \omega_s t$, then the fundamental harmonic of the reflection coefficient is given by

$$\Gamma_0 = \frac{1}{T_s} \int_{t=0}^{T_s} e^{-2jt \tan^{-1}(A \cos \omega_s t)} dt = \frac{2}{\sqrt{1+A^2}} - 1. \quad (83)$$

When $A = \sqrt{3}$, the fundamental harmonic of the reflection coefficient (and thus the RF carrier frequency of the reflected field) goes to zero. Now suppose we add a spatial dependence to the modulation function in the form of a continuous traveling-wave, i.e. $C(t) \rightarrow C(t - xT_s/d_x)$ where d_x is the spatial modulation period. In this case, when $A = \sqrt{3}$, there should not be any power radiated at the fundamental frequency nor in the specular direction. In other words, the reflected wave is completely redistributed in frequency and spatial spectrum. From Fig. 12, we observe that the reflected power at the RF carrier frequency is zero. Since $\nu = 0$ corresponds to the only frequency which radiates in the specular direction, we can also conclude that no power is reflected back at the specular angle of 25° . In the MoM simulation, the current expansion included $M = 301$ spatial samples and $U = 101$ frequency harmonics. The expansion in (80) used by the spectral-domain method was truncated at $p' = \pm 75$ and $\nu = \pm 50$. The error energy between the MoM and spectral-domain solvers is $\Delta(\bar{E}^{(MoM)}, \bar{E}^{(Spec)}) = 4.4 \times 10^{-6}$ for TE_z polarization and $\Delta(\bar{E}^{(MoM)}, \bar{E}^{(Spec)}) = 4.0 \times 10^{-4}$ for TM_z polarization.

V. CONCLUSION

As research into traveling-wave modulated structures progresses, it is vital to develop accurate computational methods capable of efficiently simulating practical designs. Typically, spatially-discrete traveling-wave modulation (SD-TWM) is employed in the physical implementation of traveling-wave modulated structures. In each spatial period (i.e. supercell) of a SD-TWM structure, a staggered modulation signal is applied to a discrete array of sub-cells (i.e. stixels). Unlike

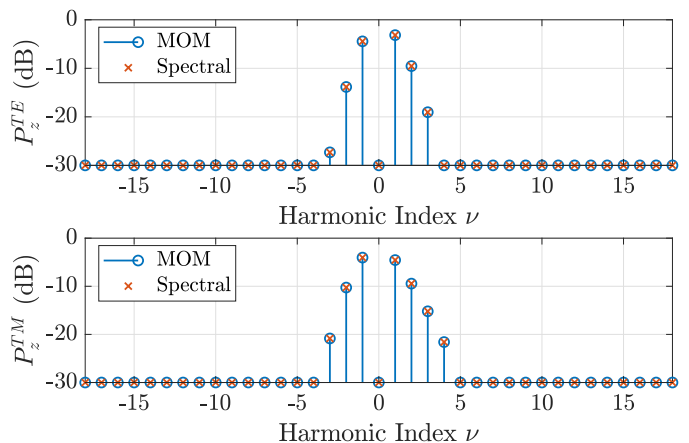


Fig. 12: Normal power radiated at each frequency $f_0 + \nu f_s$ from the metasurface in Fig. 6 modulated as specified in case C of Table I. Since this example is approaching continuous modulation, each frequency propagates in a unique direction. As a result, this modulation scheme depletes the fundamental frequency f_0 as well as the specular reflection from the scattered field.

the continuous limit, where closed form solutions are often available, numerical methods must be used to analyze SD-TWM. Due to the complicated space-time dependence of SD-TWM structures, fine discretization is required to obtain an adequate model. Further, the computational methods reported to date require the computational domain to extend in space over an entire supercell. As a result, the computational cost can become prohibitive; particularly for simulating complex patterned structures or nearly continuous structures with a large number of stixels per supercell. However, by taking advantage of the space-time symmetry of SD-TWM structures, we have shown that the fields within a single stixel determine the entire problem. Therefore, the computational domain can be reduced from an entire supercell to a single stixel. The simplicity of adding this symmetry to computational electromagnetic solvers will enable researchers to study SD-TWM for a wide variety of designs.

In this paper, a relation between neighboring stixels of a SD-TWM structure was derived and incorporated into a method of moments analysis. The derived boundary condition, referred to as the interpath relation, can be interpreted as a modified frequency-harmonic-dependent periodic boundary condition. Using the interpath relation, the fields within a single stixel are sufficient to solve the entire domain. It was shown that the interpath relation can be incorporated into a method of moments solver by slightly modifying the basis functions used to expand the surface current. As a result the number of unknowns required to solve the problem are reduced by a factor of L , the number of stixels in a supercell. The method was applied to a SD-TWM sheet capacitance over a grounded dielectric and benchmarked against a spectral-domain solver. Various SD-TWM examples were explored to both motivate and validate the proposed method.

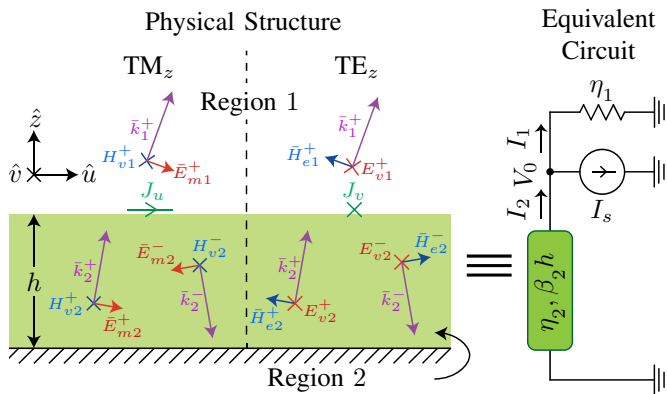


Fig. 13: An illustration of a grounded dielectric and its equivalent circuit model when excited by planar current sheets of the form $\vec{J}_0 e^{-j(k_x x + k_y y)}$. The \hat{u} axis is defined to be along the direction of $k_x \hat{x} + k_y \hat{y}$. Thus, the \hat{u} component of \vec{J}_0 excites TM_z waves, while the \hat{v} component of \vec{J}_0 excites TE_z waves.

APPENDIX A

DERIVATION OF THE SPECTRAL-DOMAIN DYADIC GREEN'S FUNCTION FOR A GROUNDED DIELECTRIC

To obtain the dyadic Green's function used in the MoM formulation, we will impress current sheets of the form $\vec{J}_0 e^{-j(k_x x + k_y y)}$ on the surface of the grounded dielectric as shown in Fig. 13. We will define region 1 to be free space and region 2 to be the dielectric substrate. As discussed in Section III, the substrate has a thickness h and a dielectric constant of ϵ_r . Further, we define $\vec{k}_\rho = k_x \hat{x} + k_y \hat{y}$. This allows us to define two orthogonal vectors \hat{u} and \hat{v} such that TM_z and TE_z excitations can be handled independently. The unit vector \hat{v} is defined to be orthogonal to \vec{k}_ρ , and is given by

$$\hat{v} = \frac{\hat{z} \times \vec{k}_\rho}{|\hat{z} \times \vec{k}_\rho|}. \quad (84)$$

The unit vector \hat{u} is defined to be orthogonal to \hat{v} and \hat{z} (i.e. \hat{u} is the unit vector in the direction of \vec{k}_ρ), and is given by

$$\hat{u} = \hat{v} \times \hat{z} = \frac{\vec{k}_\rho}{|\vec{k}_\rho|}. \quad (85)$$

We will decompose \vec{J}_0 into two orthogonal components. The component $J_u = \vec{J}_0 \cdot \hat{u}$ excites TM_z waves, while $J_v = \vec{J}_0 \cdot \hat{v}$ excites TE_z waves. Since E_u depends only on J_u and E_v depends only on J_v , the Green's function will be a diagonal tensor in the u - v coordinate system. The Green's function is defined such that [27]

$$\vec{E}_{0t} = -jk_0 Z_0 \vec{G}(k_x, k_y) \vec{J}_0, \quad (86)$$

where $\vec{E}_{0t} e^{-j(k_x x + k_y y)}$ is the component of the electric field produced by the impressed current in the x - y plane.

The fields excited in both regions can be decomposed into plane waves. In region 1, only upward-traveling waves are excited since the medium is unbounded from above. Meanwhile, in region 2, both upward- and downward-traveling waves are excited by the current sheets. When J_u is non-zero, TM_z waves are excited in regions 1 and 2. As shown

TABLE II: TM_z and TE_z Substitutions

TM_z	TE_z
$I_s = J_u$	$I_s = J_v$
$\beta_1 = \sqrt{k_0^2 - \vec{k}_\rho ^2}$	$\beta_1 = \sqrt{k_0^2 - \vec{k}_\rho ^2}$
$\eta_1 = \frac{\beta_1}{\omega \epsilon_0} = Z_0 \frac{\beta_1}{k_0}$	$\eta_1 = \frac{\omega \mu_0}{\beta_1} = Z_0 \frac{k_0}{\beta_1}$
$\beta_2 = \sqrt{\epsilon_r k_0^2 - \vec{k}_\rho ^2}$	$\beta_2 = \sqrt{\epsilon_r k_0^2 - \vec{k}_\rho ^2}$
$\eta_2 = \frac{\beta_2}{\omega \epsilon_r \epsilon_0} = Z_0 \frac{\beta_2}{\epsilon_r k_0}$	$\eta_2 = \frac{\omega \mu_0}{\beta_2} = Z_0 \frac{k_0}{\beta_2}$
$\hat{u} \cdot \vec{E}_{0t} = V_0$	$\hat{v} \cdot \vec{E}_{0t} = V_0$

in Fig. 13, the magnetic field for this excitation contains a single component along the \hat{v} direction; while the electric field contains components along both the \hat{u} and \hat{z} directions. Conversely, when J_v is non-zero, TE_z waves are excited in regions 1 and 2. As shown in Fig. 13, the electric field for this excitation contains a single component along the \hat{v} direction; while the magnetic field contains components along both the \hat{u} and \hat{z} directions.

For both the TM_z and TE_z cases, a transmission line model can be used to find the transverse component of electric field at the interface between regions 1 and 2 [29]. As shown in Fig 13, the transmission line model contains a shorted transmission line representing region 2, a current source representing the impressed current at the interface, and a load representing region 1. Using this model, computing the transverse component of electric field at the interface simply becomes a matter of finding V_0 in the equivalent circuit shown in Fig. 13. For TM_z excitations, we set $I_s = J_u$ and make the substitutions provided in the first column of Table II. The transverse component of electric field in the \hat{u} direction is found by computing V_0 . For TE_z excitations, we set $I_s = J_v$ and make the substitutions provided in the second column of Table II. The transverse component of electric field in the \hat{v} direction is found by computing V_0 .

It is clear that, for either TM_z or TE_z excitations, we must solve for V_0 in the equivalent circuit shown in Fig. 13. The impedance looking into the shorted transmission line is given by $Z_2 = j\eta_2 \tan \beta_2 h$. Therefore, the total impedance, Z_t , seen by the source is a parallel combination of η_1 and Z_2 , given by

$$Z_t = \frac{Z_0}{\frac{Z_0}{\eta_1} - j \frac{Z_0}{\eta_2} \cot \beta_2 h}. \quad (87)$$

Substituting the expressions for η_1 and η_2 from Table II into (87), we obtain

$$Z_t^{\text{TM}_z} = \frac{Z_0}{\frac{k_0}{\beta_1} - j \frac{\epsilon_r k_0}{\beta_2} \cot \beta_2 h} \quad (88)$$

$$Z_t^{\text{TE}_z} = \frac{Z_0}{\frac{\beta_1}{k_0} - j \frac{\beta_2}{k_0} \cot \beta_2 h}. \quad (89)$$

Since $V_0 = -Z_t I_s$ (the minus sign is due to the orientation of I_s), the u - v components of \vec{E}_{0t} can be computed as

$$\hat{u} \cdot \vec{E}_{0t} = -jk_0 Z_0 G_u J_u \quad (90)$$

$$\hat{v} \cdot \vec{E}_{0t} = -jk_0 Z_0 G_v J_v, \quad (91)$$

where

$$G_u = \frac{1/jk_0}{\frac{k_0}{\beta_1} - j\frac{\epsilon_r k_0}{\beta_2} \cot \beta_2 h} \quad (92)$$

$$G_v = \frac{1/jk_0}{\frac{\beta_1}{k_0} - j\frac{\beta_2}{k_0} \cot \beta_2 h}. \quad (93)$$

In these expressions, G_u and G_v represent the dyadic Green's function in the u - v coordinate system. To obtain \vec{G} in the x - y coordinate system, we first define ψ such that $\tan \psi = k_y/k_x$.

We can subsequently write \vec{G} as

$$\vec{G}(k_x, k_y) = R(\psi) \begin{bmatrix} G_u & 0 \\ 0 & G_v \end{bmatrix} R(-\psi), \quad (94)$$

where $R(\psi)$ is the rotation matrix given by

$$R(\psi) = \begin{bmatrix} \cos \psi & -\sin \psi \\ \sin \psi & \cos \psi \end{bmatrix}. \quad (95)$$

Carrying out the matrix multiplication yields the following expressions for the elements of $\vec{G}(k_x, k_y)$:

$$\hat{x} \cdot \vec{G}(k_x, k_y) \cdot \hat{x} = G_u \cos^2 \psi + G_v \sin^2 \psi \quad (96)$$

$$\hat{y} \cdot \vec{G}(k_x, k_y) \cdot \hat{y} = G_u \sin^2 \psi + G_v \cos^2 \psi \quad (97)$$

$$\begin{aligned} \hat{x} \cdot \vec{G}(k_x, k_y) \cdot \hat{y} &= \hat{y} \cdot \vec{G}(k_x, k_y) \cdot \hat{x} \\ &= \cos \psi \sin \psi (G_u - G_v). \end{aligned} \quad (98)$$

Thus the spectral-domain dyadic Green's function has been derived.

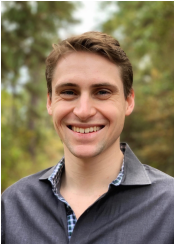
ACKNOWLEDGMENT

This work was supported under the AFOSR MURI program FA9550-18-1-0379.

This research was supported in part by the computational resources and services provided by Advanced Research Computing at the University of Michigan in Ann Arbor, Michigan.

REFERENCES

- [1] Z. Wu, C. Scarborough, and A. Grbic, "Theoretical and experimental investigations of spatio-temporally modulated metasurfaces with spatial discretization," *arXiv:2006.06394*, June 2020.
- [2] Z. Wu and A. Grbic, "Serrrodyne frequency translation using time-modulated metasurfaces," *IEEE Transactions on Antennas and Propagation*, vol. 68, no. 3, pp. 1599–1606, 2020.
- [3] Y. Vahabzadeh, N. Chamanara, K. Achouri, and C. Caloz, "Computational analysis of metasurfaces," *IEEE Journal on Multiscale and Multiphysics Computational Techniques*, vol. 3, pp. 37–49, 2018.
- [4] D. Sarkar, C. Scarborough, Z. Wu, and A. Grbic, "Time-varying phase control for frequency translation," in *2019 IEEE International Symposium on Antennas and Propagation and USNC-URSI Radio Science Meeting*. IEEE, 2019, pp. 1113–1114.
- [5] E. S. Cassedy and A. A. Oliner, "Dispersion relations in time-space periodic media: Part i—stable interactions," *Proceedings of the IEEE*, vol. 51, no. 10, pp. 1342–1359, Oct 1963.
- [6] P. Tien and H. Suhl, "A traveling-wave ferromagnetic amplifier," *Proceedings of the IRE*, vol. 46, no. 4, pp. 700–706, 1958.
- [7] P. Tien, "Parametric amplification and frequency mixing in propagating circuits," *Journal of Applied Physics*, vol. 29, no. 9, pp. 1347–1357, 1958.
- [8] H. Heffner and G. Wade, "Gain, band width, and noise characteristics of the variable-parameter amplifier," *Journal of Applied Physics*, vol. 29, no. 9, pp. 1321–1331, 1958.
- [9] N. Reiskarimian and H. Krishnaswamy, "Magnetic-free non-reciprocity based on staggered commutation," *Nature Commun.*, vol. 7, no. 11217, 2016.
- [10] A. E. Cardin, S. R. Silva, S. R. Vardeny, W. J. Padilla, A. Saxena, A. J. Taylor, W. J. Kort-Kamp, H.-T. Chen, D. A. Dalvit, and A. K. Azad, "Surface-wave-assisted nonreciprocity in spatio-temporally modulated metasurfaces," *Nature communications*, vol. 11, no. 1, pp. 1–9, 2020.
- [11] Y. Mazor and A. Alú, "One-way hyperbolic metasurfaces based on synthetic motion," *IEEE Transactions on Antennas and Propagation*, vol. 68, no. 3, pp. 1739–1747, 2020.
- [12] M. M. Salary, S. Jafar-Zanjani, and H. Mosallaei, "Nonreciprocal optical links based on time-modulated nanoantenna arrays: Full-duplex communication," *Phys. Rev. B*, vol. 99, p. 045416, Jan 2019. [Online]. Available: <https://link.aps.org/doi/10.1103/PhysRevB.99.045416>
- [13] S. Rudolph, "Broadband, volumetric negative-refractive-index media," Ph.D. dissertation, The University of Michigan, 1301 Beal Ave, Ann Arbor, MI 48109, 2011.
- [14] A. M. Shaltout, V. M. Shalaev, and M. L. Brongersma, "Spatiotemporal light control with active metasurfaces," *Science*, vol. 364, no. 6441, 2019.
- [15] T. Shan, X. Pan, M. Li, S. Xu, and F. Yang, "Coding programmable metasurfaces based on deep learning techniques," *IEEE Journal on Emerging and Selected Topics in Circuits and Systems*, vol. 10, no. 1, pp. 114–125, 2020.
- [16] S. Taravati and G. V. Eleftheriades, "Generalized space-time-periodic diffraction gratings: Theory and applications," *Phys. Rev. Applied*, vol. 12, p. 024026, Aug 2019. [Online]. Available: <https://link.aps.org/doi/10.1103/PhysRevApplied.12.024026>
- [17] Y. Hadad, D. L. Sounas, and A. Alú, "Space-time gradient metasurfaces," *Phys. Rev. B*, vol. 92, p. 100304, Sep 2015. [Online]. Available: <https://link.aps.org/doi/10.1103/PhysRevB.92.100304>
- [18] S. A. Stewart, T. J. Smy, and S. Gupta, "Finite-difference time-domain modeling of space-time-modulated metasurfaces," *IEEE Transactions on Antennas and Propagation*, vol. 66, no. 1, pp. 281–292, 2018.
- [19] Z. Wu, C. Scarborough, and A. Grbic, "A spatio-temporally modulated metasurface as a free-space N-path system," in *The 14th European Conference on Antennas and Propagation (EuCAP 2020)*, 2020.
- [20] C. Scarborough and A. Grbic, "Modified floquet boundary condition for open boundary problems with N-path symmetry," in *2020 14th International Congress on Artificial Materials for Novel Wave Phenomena (Metamaterials)*, 2020.
- [21] H. A. Lorentz, "Electromagnetic phenomena in a system moving with any velocity smaller than that of light," in *Collected Papers*. Springer, 1937, pp. 172–197.
- [22] S. Young, personal communication, April, 2020.
- [23] C. Scarborough and A. Grbic, "Accelerated N-path network analysis using the floquet scattering matrix method," *IEEE Transactions on Microwave Theory and Techniques*, pp. 1–12, 2020.
- [24] J. A. Richards, *Analysis of Periodically Time Varying Systems*. New York, NY: Springer-Verlag, 1983.
- [25] C. A. Balanis, *Antenna Theory Analysis and Design*. Hoboken, New Jersey: John Wiley & Sons, Inc., 2016.
- [26] T. J. Smy and S. Gupta, "Exact finite-difference time-domain modelling of broadband huygens' metasurfaces with lorentz dispersions," *arXiv:1609.05575*, September 2016.
- [27] J.-M. Jin, *Theory and computation of electromagnetic fields*. John Wiley & Sons, 2011.
- [28] Y. S. Koshkin, E. Mukhin, G. Razdobarin, V. Semenov, A. Shilnikov, Y. K. Mihailovskij, and L. Bakh, "Lower order blaze grating spectrometer of large diffraction angle," *Review of scientific instruments*, vol. 70, no. 10, pp. 3844–3846, 1999.
- [29] A. Grbic, "EECS 598 lecture 13," Lecture Notes, 2018.



Cody Scarborough graduated from the University of Texas at Austin with a B.S. in Electrical and Computer Engineering in 2017. Throughout his undergraduate degree, he was employed at Applied Research Laboratories and subsequently at the University of Texas as an undergraduate research assistant. His work has included projects in global navigation systems, wireless communication networks for vehicular technology and the efficient computation of radiation from cryptographic integrated circuits. He is currently a graduate student pursuing a PhD at

the University of Michigan, where he studies time-varying electromagnetic structures and metamaterials. His research interests include the study of wave phenomena, non-linear electronic devices, solid-state physics, spatio-temporal modulation, microwave systems and optics.



Zhanni Wu received the B.S. degree from the School of Information Science and Engineering, Southeast University, Nanjing, China, in 2015, and the M.S.E. degree from the University of Michigan, Ann Arbor, MI, USA, in 2017, where she is currently pursuing the Ph.D. degree in electrical engineering. She was with the State Key Laboratory of Millimeter Waves, Southeast University, from 2013 to 2015, as an Undergraduate Research Assistant. Her current research interests include metamaterials/metasurfaces, tunable metasurface devices, and

wave propagation in spatio-temporal modulated metamaterials.



Anthony Grbic received the B.A.Sc., M.A.Sc., and Ph.D. degrees in electrical engineering from the University of Toronto, Toronto, ON, Canada, in 1998, 2000, and 2005, respectively. In January 2006, he joined the Department of Electrical Engineering and Computer Science, University of Michigan, Ann Arbor, MI, USA, where he is currently a Professor. His research interests include engineered electromagnetic structures (metamaterials, metasurfaces, electromagnetic band-gap materials, frequency-selective surfaces), plasmonics, antennas, microwave circuits,

wireless power transmission, and analytical electromagnetics/optics.

Dr. Grbic served as Technical Program Co-Chair in 2012 and Topic CoChair in 2016 and 2017 for the IEEE International Symposium on Antennas and Propagation and USNC-URSI National Radio Science Meeting. He was an Associate Editor for IEEE Antennas and Wireless Propagation Letters from 2010 to 2015. He is currently the Vice Chair of AP-S Technical Activities, Trident Chapter, IEEE Southeastern Michigan Section. Dr. Grbic was the recipient of AFOSR Young Investigator Award as well as NSF Faculty Early Career Development Award in 2008, the Presidential Early Career Award for Scientists and Engineers in January 2010. He also received an Outstanding Young Engineer Award from the IEEE Microwave Theory and Techniques Society, a Henry Russel Award from the University of Michigan, and a Booker Fellowship from the United States National Committee of the International Union of Radio Science in 2011. He was the inaugural recipient of the Ernest and Bettine Kuh Distinguished Faculty Scholar Award in the Department of Electrical and Computer Science, University of Michigan in 2012.